

Parsec-scale structures and diffuse bands in a translucent interstellar medium at $z \simeq 0.079$ *

R. Srianand¹†, N. Gupta², H. Rahmani¹, E. Momjian³, P. Petitjean⁴ and P. Noterdaeme⁴

¹ IUCAA, Postbag 4, Ganeshkhind, Pune 411007, India

² Netherlands Institute for Radio Astronomy (ASTRON), Postbus 2, 7990 AA, Dwingeloo, The Netherlands

³ National Radio Astronomy Observatory, 1003 Lopezville Road, Socorro, NM 87801, USA

⁴ Institut d'Astrophysique de Paris, UPMC-CNRS, UMR7095, 98bis Boulevard Arago, 75014 Paris, France

Accepted. Received; in original form

ABSTRACT

We present a detailed study of the QSO-galaxy pair [SDSS J163956.35+112758.7 ($z_q = 0.993$) and SDSS J163956.38+112802.1 ($z_g = 0.079$)] based on observations carried out using the Giant Meterwave Radio Telescope (GMRT), the Very Large Baseline Array (VLBA), the Sloan Digital Sky Survey (SDSS) and the ESO New Technology Telescope (NTT). We show that the interstellar medium of the galaxy probed by the QSO line of sight has near-solar metallicity ($12+\log(\text{O}/\text{H}) = 8.47\pm 0.25$) and dust extinction ($E(\text{B}-\text{V}) \sim 0.83\pm 0.11$) typical of what is usually seen in translucent clouds. We report the detection of absorption in the $\lambda 6284$ diffuse interstellar band (DIB) with a rest equivalent width of $1.45\pm 0.20\text{\AA}$. Our GMRT spectrum shows a strong 21-cm absorption at the redshift of the galaxy with an integrated optical depth of $15.70\pm 0.13 \text{ km s}^{-1}$. Follow-up VLBA observations show that the background radio source is resolved into three components with a maximum projected separation of 89 pc at the redshift of the galaxy. One of these components is too weak to provide useful 21-cm H I information. The integrated H I optical depth towards the other two components are higher than that measured in our GMRT spectrum and differ by a factor 2. By comparing the GMRT and VLBA spectra we show the presence of structures in the 21-cm optical depth on parsec scales. We discuss the implications of such structures for the spin-temperature measurements in high- z damped Lyman- α systems. The analysis presented here suggests that this QSO-galaxy pair is an ideal target for studying the DIBs and molecular species using future observations in optical and radio wavebands.

Key words: quasars: active – quasars: absorption lines – quasars: individual: SDSS J163956.35+112758.7 – ISM: lines and bands – ISM: molecules

1 INTRODUCTION

Understanding parsec scale H I opacity fluctuations in the interstellar medium (ISM) of galaxies and how they depend on the feedback from in situ star formation is very important. In the Galaxy, the radio observations of H I 21-cm absorption towards high-velocity pulsars and extended radio sources, the optical observations of Na I absorption

lines towards globular clusters and binary stars have shown that the diffuse ISM is structured on parsec to sub-parsec ($\sim 10\text{AU}$) scales (Frail et al. 1994; Bates et al. 1995; Heiles 1997; Deshpande 2000; Rollinde et al. 2003; Boissé et al. 2005; Brogan et al. 2005; Roy et al. 2012). These small-scale structures, due to large over-pressures, cannot survive rapid evaporation in the standard pressure-equilibrium based models (see for example, McKee & Ostriker 1977) and therefore raises many important questions regarding the nature of the ISM. It is possible that these are transient phases controlled by turbulence (Mac Low & Klessen 2004).

Physical conditions in H I gas associated with high redshift galaxies can be probed by 21-cm absorption. In particular, the H I 21-cm optical depth combined with a deter-

* Based on data obtained with EFOSC2 at the NTT of the European Southern Observatory (Prgm. ID: 085.A-0709(A); PI: Rahmani), VLBA (Prgm ID:BG208; PI: Gupta) and GMRT (Prgm. ID: 18-074 and 20-037, PI: Gupta)

† E-mail: anand@iucaa.ernet.in

mination of $N(\text{H I})$ from Lyman- α absorption yield an estimate of the spin temperature, T_S , (Kanekar & Chengalur 2003) which is a good indicator of the kinetic temperature (Roy et al. 2006). However, to fully interpret high redshift 21-cm spin-temperature measurements one needs to know the parsec scale structure of the H I gas. In turn, if radio emission of the background QSO has structures at different scales then Very Large Baseline Interferometry (VLBI) spectroscopy can be used to probe the spatial variations of the H I gas opacity.

Due to limitations of existing facilities, VLBI spectroscopic observations of QSO absorbers are limited to low-redshifts only. In the case of the $z_{\text{abs}} = 0.0912$ DLA towards B0738+313, Lane et al. (2000) found the background source to be partially resolved at milliarcsec (mas) scales. Within the measurement uncertainties they do not find any strong variations in the H I optical depth across 20 pc. The associated galaxy could be a low surface brightness dwarf at an impact parameter of ≤ 3.5 kpc without any signature of ongoing star formation (see Turnshek et al. 2001). In the case of the $z = 0.03321$ galaxy towards J104257.58+074850.5, the background radio source is unresolved in the Very Large Baseline Array (VLBA) image and the 21-cm absorption is found to be similar over 27.1×13.9 pc (see Borthakur et al. 2010, for details). Note that the impact parameter in this case is 1.7 kpc and the foreground galaxy is a low luminosity spiral with low gas phase metallicity and dust extinction along the QSO sight line.

Alternatively, time variability of 21-cm absorption is seen in two cases [the absorbers towards B0235+164 (Wolfe et al. 1982) and B1127-145 (Kanekar & Chengalur 2001)] suggesting that the H I gas is patchy on pc scales. Interestingly, the $z_{\text{abs}} = 0.524$ absorption system towards B0235+164 is one of the extra-galactic systems that shows Diffuse Interstellar Bands (DIBs; Junkkarinen et al. 2004). Using a large sample of $z \leq 1.5$ Mg II absorbers searched for 21-cm absorption together with mas scale radio images Gupta et al. (2012), have concluded that the H I gas is patchy with a typical correlation length of 30–100 pc based on different correlation analyses.

It has been shown that, like 21-cm absorption, one can use H₂ absorption to probe the cold neutral medium (CNM) in $z \geq 1.8$ damped Lyman- α systems (DLAs; Ledoux et al. 2003; Srianand et al. 2005; Noterdaeme et al. 2008). Recently Balashev et al. (2011), using partial coverage arguments, derived the linear size of the H₂-bearing core and the H I envelope to be $0.15^{+0.05}_{-0.05}$ pc and $8.2^{+6.5}_{-4.1}$ pc respectively for the $z_{\text{abs}} = 2.3377$ DLA towards Q1232+082. Srianand et al. (2012), combining 21-cm and H₂ information for a sample of high- z DLAs, concluded that the typical size of H₂ bearing clouds is ≤ 15 pc.

All this indicates that the ISM of high- z galaxies is structured on parsec scales. However, most of the evidences are based on indirect arguments. In addition one would like to connect the structures seen in H I to other observable properties of the galaxy such as metallicity, dust content, local star formation etc. We are performing a systematic search for 21-cm and OH absorption in a well selected sample of Quasar-galaxy pairs (QGP, a fortuitous alignment of a foreground visible galaxy with a distant background quasar) with impact parameter $b \leq 20$ kpc. In case of detection we also perform optical long-slit and VLBA spectroscopic

Table 1. Emission line parameters of the galaxy SDSS J163956.38+112802.1

| Line(l) | $F_\lambda (10^{-17} \text{ erg s}^{-1} \text{ cm}^{-2})$ | $F_\lambda(\text{H}\alpha)/F_\lambda$ |
|------------------------|---|---------------------------------------|
| H α | 147.0 \pm 2.9 | 1.00 |
| H β | 33.3 \pm 1.8 | 4.41 \pm 0.26 |
| [O II] λ 3728 | 75.3 \pm 4.1 | 1.95 \pm 0.11 |
| [O III] λ 4960 | 15.9 \pm 1.4 | 9.25 \pm 0.82 |
| [O III] λ 5008 | 42.9 \pm 1.8 | 3.42 \pm 0.16 |
| [N II] λ 6549 | 6.3 \pm 1.2 | 23.17 \pm 4.55 |
| [N II] λ 6585 | 28.7 \pm 1.8 | 5.11 \pm 0.34 |
| [S II] λ 6718 | 28.5 \pm 1.7 | 5.16 \pm 0.33 |
| [S II] λ 6732 | 20.3 \pm 1.5 | 7.24 \pm 0.55 |

follow-up observations. Initial results from the GMRT observations of 5 QGPs, with the redshift of the galaxies in the range $0.03 \leq z_g \leq 0.18$ are presented in Gupta et al. (2010).

Here we present a detailed analysis of a very special QGP with the background QSO (J163956.35+112756.7, $z_q = 0.993$) sight line piercing through the optical disk (Fig. 1) of the foreground galaxy (J163956.38+112802.1, $z_g = 0.079$ or corresponding heliocentric velocity of $v_{\text{helio}} \sim 23710$ km s⁻¹). We report the detection of 21-cm, Na I absorption and DIBs in this galaxy. We use a long slit spectrum to study the star formation rate, metallicity and rotation curve of the galaxy. The background radio source is well resolved at mas scales. We present the VLBA spectroscopy and discuss the parsec scale structures in the H I gas. We will use a flat cosmological model with $\Omega_m = 0.27$, $h = 0.70$ (Komatsu et al. 2009).

2 PHYSICAL CONDITIONS IN THE GALAXY

2.1 Metallicity and dust in the emission line regions

Strong emission lines from the foreground galaxy are seen in the SDSS spectrum (see Fig. 1). They suggest the presence of a star forming region within a projected separation of 2.2 kpc to the QSO sightline¹. We fit the emission lines using Gaussians and the integrated line fluxes are summarised in Table 1. A luminosity distance of 354.1 Mpc is used to convert these fluxes into luminosities. The last column in this table gives the ratio of the H α flux with respect to that of other emission lines. Following Argence & Lamareille (2009), we derive the optical depth in the systemic V-band of the galaxy, $\tau_V^{\text{Balmer}} = 1.39^{+0.18}_{-0.19}$, using the observed H α /H β ratio, the intrinsic Balmer ratio of 2.85 (Osterbrock & Ferland 2006) and the wavelength dependence of the dust optical depth (i.e τ_λ) as given by Eq. 3 of Wild et al. (2007). We estimate a dust uncorrected surface density of the star formation rate (SFR) of $0.006 \text{ M}_\odot \text{ yr}^{-1} \text{ kpc}^{-2}$. Applying the dust correction will increase this estimate by a factor of three for τ_V^{Balmer} quoted above. If we assume that this

¹ The SDSS fiber has a diameter of 3 arcsec and was centered on the QSO. An angular scale of 1 arcsec corresponds to a projected size of 1.474 kpc at the redshift of the galaxy. Therefore, the SDSS spectrum is the juxtaposition of the QSO spectrum with that of the galaxy within a radius of 2.2 kpc.

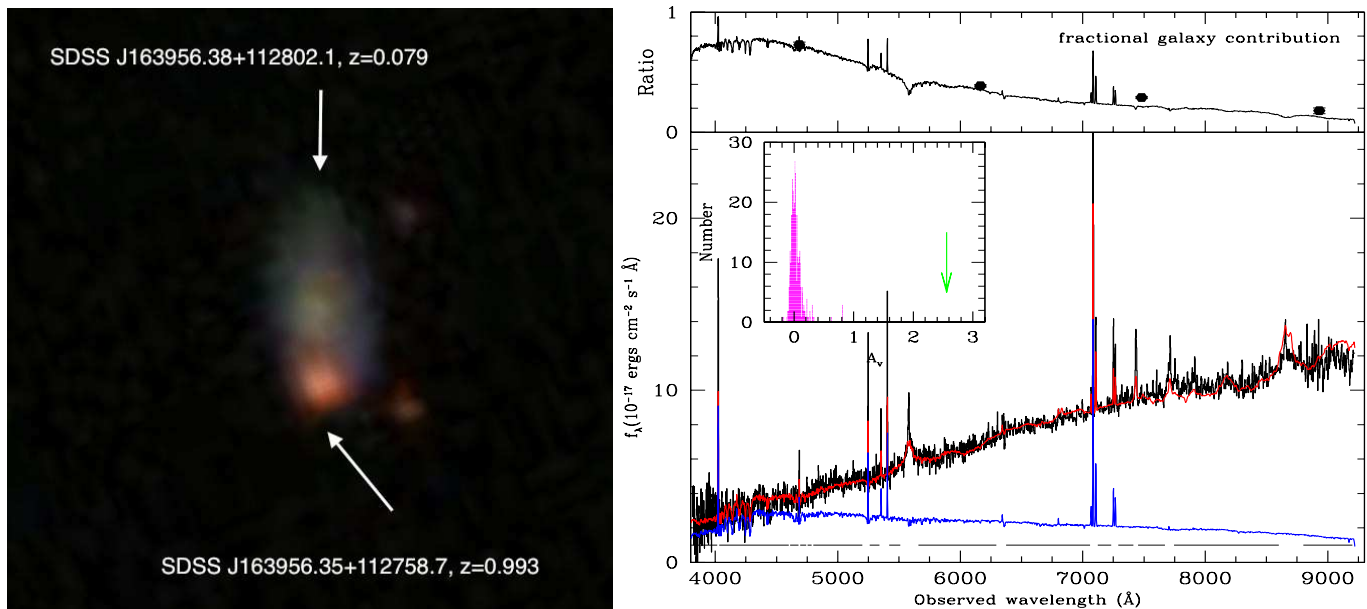


Figure 1. *Left:* SDSS colour image ($30'' \times 30''$) showing the QSO (SDSS J163956.35+112758.7, $z_q = 0.993$) sight line piercing through the disk/spiral-arm of the foreground galaxy (SDSS J163956.38+112802.1, $z_g = 0.079$) *Right:* The SDSS spectrum of the QSO is fitted with a combination of a reddened QSO composite spectrum and a spiral galaxy template (blue spectrum) from SDSS. The insert gives the distribution of A_V measured for a control sample of QSOs with similar redshift as Q1639+1127. The arrow marks the measured A_V in the present case. In the top right panel we show the relative contribution of the galaxy light to the SDSS spectrum as a function of wavelength. This contribution derived in different bands from SDSS images are also plotted as big black points.

disk galaxy obeys the Kennicutt-Schmidt law then we get $N(\text{H I}) \sim 2.6 \times 10^{21} \text{ cm}^{-2}$ using the best fitted parameters of Kennicutt (1998a,b). Using the measured O3N2 ratio (i.e. $\log [F_\lambda(\text{O III } \lambda 5007)/F_\lambda(\text{H}\beta) \div F_\lambda([\text{N II}] \lambda 6585)/F_\lambda(\text{H}\alpha)]$) and the best fitted relationship given in Pettini & Pagel (2004) we get, $12 + \log (\text{O}/\text{H}) = 8.47 \pm 0.25$. Thus the QSO sightline is passing close to (i.e. within 2.2 kpc) a star forming region having near-solar metallicity and high $N(\text{H I})$.

2.2 Modelling the QSO spectral energy distribution

The background QSO spectrum is highly reddened (see Fig. 1). We get an independent estimate of τ_V and $E(\text{B}-\text{V})$ by fitting the QSO spectral energy distribution (SED) using,

$$f_\lambda = A f_Q^{\lambda_1} e^{-\tau_{\lambda_2}} + B f_g^{\lambda_2}. \quad (1)$$

Here f_λ , $f_Q^{\lambda_1}$ and $f_g^{\lambda_2}$ are, respectively, the observed flux at λ , the flux in the QSO composite spectrum at $\lambda_1 = \lambda(1+z_q)$ and the flux in the galaxy continuum that also enters the SDSS fiber. We approximate the latter with a spiral galaxy template at $\lambda_2 = \lambda(1+z_g)$. A and B are normalization factors and z_q and z_g are the redshifts of the QSO and the foreground galaxy respectively. The form of τ_λ is taken from the Milky Way extinction curve (Fitzpatrick & Massa 1988). The fitting method used is very similar to the one used in Srianand et al. (2008) and Noterdaeme et al. (2009). As can be seen from the right panel of Fig. 1, the best fit (with $\chi_\nu^2 = 1.23$) to the observed spectrum is obtained for

$A_V = 2.56 \pm 0.02$ (with $E(\text{B}-\text{V}) = 0.82 \pm 0.01$ and $R_V = 3.1$)², where $A_\lambda = 1.086 \tau_\lambda$. The quoted errors are mainly statistical ones. In Fig. 1 we also show the distribution of A_V obtained for a control sample of SDSS QSOs with $z \sim z_q$. For this exercise we do not consider the foreground galaxy contribution to the SED (i.e. the second term in Eq. 1). The rms of the A_V distribution of 0.11 reflects a typical systematic error in the SED fitting method due to the dispersion of the QSO unreddened spectral energy distribution. Therefore, the reddening noted in the present case is significant at more than the 20σ level. The measured value of A_V is consistent with the line of sight passing through a translucent region [defined as a region with $1 \leq A_V \leq 10$ (van Dishoeck & Black 1989; Snow & McCall 2006)]. If we use the relationship between $N(\text{H I})$ and A_V derived in the Galactic ISM (Bohlin et al. 1978) then the above inferred A_V is consistent with $N(\text{H I}) = 4 \times 10^{21} \text{ cm}^{-2}$. The difference between the two A_V estimates obtained using the Balmer decrement (i.e. $A_V^{\text{Balmer}} = 1.51_{-0.18}^{+0.19}$) and the fit of the QSO SED can be attributed to differences in the dust opacity (or differences in $N(\text{H I})$, if we assume uniform dust-to-gas ratio) towards the QSO and the H α emitting regions. In passing, we wish to point out that the line of sight discussed here has more dust opacity than any of the high- z dusty Mg II and CO systems that also produce 2175 Å absorption (Srianand et al. 2008; Noterdaeme et al. 2009; Jiang et al. 2011).

The SED fitting procedure used above predicts the relative contributions of the QSO and the galaxy as a function

² The derived value of $E(\text{B}-\text{V})$ depends on our choice of R_V . In the absence of R_V measurement we adopt $R_V = 3.1$ as seen in the Milky Way.

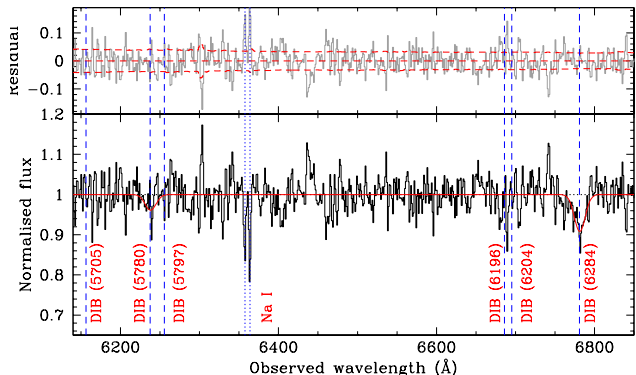


Figure 2. NTT spectrum of the QSO. Vertical dotted and dashed lines mark the positions of Na D lines and DIBs respectively. A strong absorption is seen at the expected position of the $\lambda 6284$ DIB. The best gaussian profile fitted to this feature is shown together with the absorption in the $\lambda 5780$ Å DIB expected from the correlation found by Friedman et al. (2011) in the Galactic ISM. *Top-panel:* Residual flux after subtracting the Gaussian fits from the observed spectrum. The 1σ range from the error spectrum (horizontal dashed line) is also shown.

of wavelength (top right panel in Fig. 1). We independently estimate this ratio at different wavelengths using different SDSS broad band images within an aperture of $1.5''$ centered at the position of the quasar. We use the following steps: 1) cut an image stamp of 80 pixels on a side around the QGP, 2) subtract a constant background obtained by averaging the counts in more than 10 neighboring regions close to the pair, 3) obtain the radial surface brightness profile of the galaxy (after masking the quasar) by fitting isophotal ellipses using STSDAS package in IRAF, 4) derive the total counts due to the galaxy within an aperture of 1.5 arcsec radius at the location of the quasar using the fitted isophots. The estimated ratios together with the errors (mainly from Poisson statistics) are also shown in the top-right panel of Fig. 1. They are very much consistent with the curve obtained from the SED fitting. This confirms the robustness of our fitting procedure. In addition, based on the ellipticity of the outer isophots in the r and i bands, we measure a disk inclination angle of ~ 63 deg.

2.3 Na I absorption

Using the European Southern Observatory (ESO) New Technology Telescope (NTT), we performed long-slit spectroscopic observations of the QSO-galaxy pair aligning the slit (of width 1.2 arcsec and length 4.1 arcmin) along the semi-major axis of the galaxy. The spectra (4×2700 s exposures) were obtained in good seeing conditions (~ 0.8 arcsec) using the ESO Faint Object Spectrograph and Camera (EFOSC2) covering the wavelength range 6040–7135 Å at a spectral resolution of 200–250 km s^{-1} . The data were processed using standard IRAF³ long-slit routines. One dimensional spectra were extracted with sub-apertures having

a width of 5 pixels (i.e projected size of ~ 2 kpc). The results are summarized in Fig. 2.

In the spectra of the QSO (shown in the bottom panel in Fig. 2) we detect Na I $\lambda\lambda 5891, 5897$ lines with rest equivalent widths, $W_r = 0.65 \pm 0.10$ and 0.58 ± 0.10 Å respectively at z_g . Using the empirical relationship between $E(B-V)$ and $W(\text{Na I})$ reported recently by Poznanski et al. (2012) we estimate $E(B-V) = 0.31^{+0.41}_{-0.12}$ and $0.47^{+0.75}_{-0.29}$ from the measured equivalent widths. The $E(B-V)$ we measure from the SED fitting is higher than these values but consistent within uncertainties.

As the doublet ratio is close to 1 and the resolution of our spectrum is low it is most likely that the lines are saturated. A very conservative lower limit of $\log N(\text{Na I}) \geq 12.78$ is obtained assuming the optically thin case. Consequently we derive $N(\text{H I}) \geq 10^{21} \text{ cm}^{-2}$ from the known correlation between $N(\text{Na I})$ and $N(\text{H I})$ found in our Galaxy (Ferlet et al. 1985; Wakker & Mathis 2000).

2.4 Diffuse Interstellar Bands

All the optical observations presented above suggest that the gas along the line of sight has $N(\text{H I}) \geq 10^{21} \text{ cm}^{-2}$, with near solar metallicity and high dust content. In such cases one can expect to detect absorption from different molecular species and diffuse interstellar bands (Sarre 2006). In Fig. 2 we have marked the expected positions of DIBs using vertical dashed lines. A clear absorption is detected at the expected position of the $\lambda_r = 6284$ Å DIB. Using a Gaussian fit we measure a rest equivalent width of 1.46 ± 0.21 Å and $\text{FWHM} = 14 \pm 2$ Å. The measured FWHM is 1.4 times larger than what is seen in nearby starburst galaxies (Heckman & Lehnert 2000) and roughly a factor 2.2 higher than what is seen in the Galactic ISM towards HD 204827 (Hobbs et al. 2008). No other DIB absorption is detected at more than the 3σ significance level. We place a 3σ upper limit of 0.66 Å for the rest equivalent width of the $\lambda 5780$ DIB feature.

In the local universe DIB observations are available for the ISM of Magellanic clouds (Welty et al. 2006; Cox et al. 2006, 2007), M33 (Cordiner et al. 2008), M31 (Cordiner et al. 2011), NGC 1448 (Sollerman et al. 2005) and some nearby starburst galaxies (Heckman & Lehnert 2000). In Fig. 3 we plot $W_r(\lambda 6284)$ against $E(B-V)$ found in these cases. The strength of $\lambda 6284$ is affected by the strength of the radiation field and metallicity. Low equivalent width is explained by stronger radiation field and/or lower metallicity. It is interesting to note the metallicity measured in the present case is close to that measured in M31 and starburst galaxies studied by Heckman & Lehnert (2000). However, the equivalent width of the $\lambda 6284$ DIB is found to be higher than that predicted by the correlation found by Friedman et al. (2011). This may imply slightly low ambient radiation field along the QSO sight line. Alternatively, if we assume that the physical conditions in the galaxy studied here are similar to that of the Galactic ISM then we get $\log N(\text{H I}) = 21.76 \pm 0.25$ and $E(B-V) = 1.30 \pm 0.20$ from the observed $W_r(\lambda 6284)$ and the correlations found by Friedman et al. (2011). Interestingly the $N(\text{H I})$ value inferred here matches well, albeit with large uncertainties, with that we infer from the $A_V - N(\text{H I})$ relationship of Bohlin et al. (1978). In addition, the inferred $E(B-V)$ may mean $R_V = 1.9^{+0.4}_{-0.2}$ and not 3.1 as we have assumed before.

³ IRAF is distributed by the National Optical Astronomy Observatories, which are operated by the Association of Universities for Research in Astronomy, Inc., under cooperative agreement with the National Science Foundation.

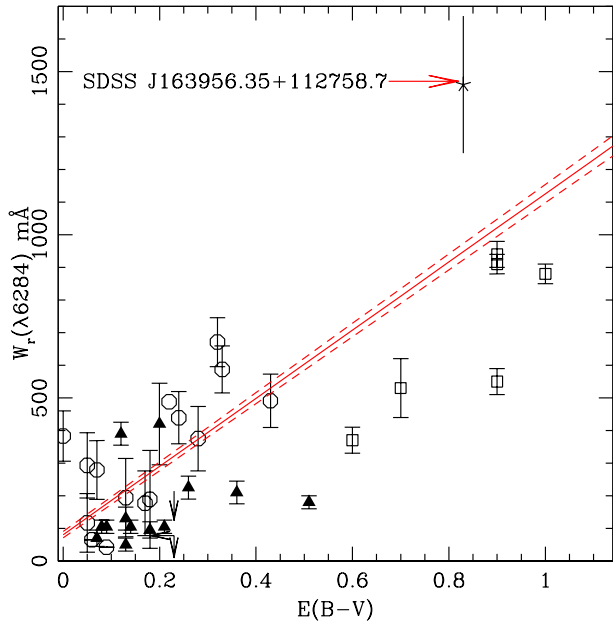


Figure 3. Comparison of $E(B-V)$ and $W_r(\lambda 6284)$ in different extra-galactic environments. The solid and dashed lines are the best fitted relationship and its 1σ error found in the milky way (Friedman et al. 2011). Filled triangles, open squares and open circles are for Magellanic clouds (Welty et al. 2006), nearby starburst galaxies (Heckman & Lehnert 2000) and M31 (Cordiner et al. 2011) respectively. The data for the present system is marked with a star.

This is similar to what has been inferred for the host galaxies of high- z supernovae (Wang et al. 2006). Therefore, it is important to have independent measurements of $N(\text{H I})$ and R_V for the present case.

In all the local measurements discussed above $W_r(\lambda 5780)$ is found to be smaller than $W_r(\lambda 6284)$. If we use the correlations found by Friedman et al. (2011), we obtain $W_r(\lambda 5780) = 0.61 \pm 0.08 \text{ \AA}$. We show the expected profile in the bottom panel of Fig. 2. From the residual plot shown in the top panel of Fig. 2 we can say that the observed spectrum is consistent with $\lambda 5780$ DIB feature having the predicted equivalent width. From Table 3 of Welty et al. (2006), we find the average value of the $W_r(\lambda 6284)/W_r(\lambda 5780)$ ratio to be 2.9 ± 0.2 in the case of the Magellanic clouds. Based on this we obtain $W_r(\lambda 5780) = 0.5 \pm 0.1 \text{ \AA}$. Detecting this feature and other DIB features in a high signal-to-noise ratio spectrum will allow us to probe the physical state of the gas in more detail.

This is only the third detection of DIBs due to intervening absorbers in QSO spectra (see Junkkarinen et al. 2004; Ellison et al. 2008). In previous cases the $\lambda 5780$ DIB was detected without clear detection of the $\lambda 6284$ DIB. This is very much contrary to what has been seen in the local universe (apart from the rare sight line towards Sk 143, as seen in Welty et al. 2006) and in the present case. York et al. (2006), by analogy with Sk143, attributed these unusual line ratios to the ISM being more protected from the ambient UV radiation field.

The present NTT spectrum does not allow us to search for molecular absorption. However, based on known corre-

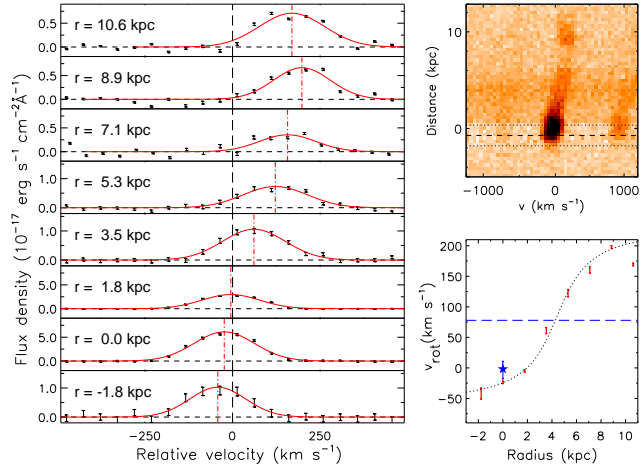


Figure 4. *Left panel:* Velocity plot showing the $\text{H}\alpha$ emission extracted at different locations in the galaxy. *Top right:* 2D spectra in the region of $\text{H}\alpha$ and $[\text{N II}]$ emission lines after subtracting the QSO light. The horizontal lines show the location of the QSO trace. *Bottom right:* the rotation curve obtained from the $\text{H}\alpha$ line. The star is the velocity of the H I gas seen in 21-cm absorption towards the QSO (see Section 3.1). The zero of the velocity scale is set at $z_{\text{abs}} = 0.0791$ and zero of the spatial scale is set at the position of the QSO.

lations in the Galactic ISM we expect $\log N(\text{CH}) \geq 13.8$, $\log N(\text{CH}^+) \geq 13.5$ and $\log N(\text{CN}) \geq 12.4$ (Welty et al. 2006). Therefore high resolution follow-up spectroscopy of this source could yield very good insights into the ISM of this external galaxy.

2.5 $\text{H}\alpha$ rotation curve

In this sub-section we study the large scale kinematics of the emission line gas using the NTT long-slit spectrum. In the left panel of Fig 4 we show the $\text{H}\alpha$ emission observed in different sub-apertures together with the best fitted Gaussian profiles. The measured FWHM is close to our spectral resolution suggesting low velocity dispersion along the line of sight. The 2D spectrum around the $\text{H}\alpha$ range after subtracting the QSO trace is shown in the right panel. While the rotation is apparent we also notice that the blue side is brighter suggesting additional star formation activity. Coincidentally the QSO sightline is very close to this star forming region. The angular separation between the center of the QSO trace and the center of the nearest star forming region (based on the peak of the $\text{H}\alpha$ emission) is 0.48 arc sec. This corresponds to a physical separation of 0.7 kpc. The different values of A_V measured toward the $\text{H}\alpha$ emitting region and the QSO reflect roughly a factor of 2 change in A_V within a projected separation of 0.7 kpc. Therefore, the projected distance (and associated dust extinction) is large enough so that the gas along the QSO sightline may not be influenced by the star-forming region. The QSO sight line is at an impact parameter of 4 kpc from the galactic center. The rotation curve plotted in Fig. 4 suggests an asymptotic circular velocity of $\sim 125 \text{ km s}^{-1}$. This circular velocity for a typical radius of 10 kpc corresponds to a dynamical mass of $\sim 4 \times 10^{10} M_{\odot}$ after correction for the inclination angle

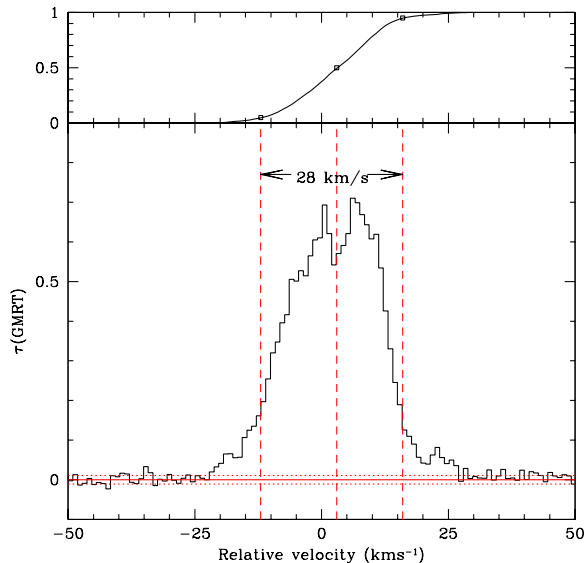


Figure 5. Optical depth profile of the 21-cm absorption towards J1639+1127 detected in the GMRT spectrum. Top panel shows the cumulative optical depth profile. The open squares (and vertical dashed lines in the bottom panel) mark the velocities at which the integrated optical depth is 5%, 50% and 95% of the total value. The mean optical depth and associated RMS in the absorption free regions are shown with solid and dotted horizontal lines respectively. The velocity scale is defined with respect to $z = 0.079098$.

of 63 deg. This suggests that the host galaxy is a low mass disk galaxy.

3 21-CM ABSORPTION AND PARSEC SCALE STRUCTURES

3.1 GMRT 21-cm spectrum

As the background QSO is radio-loud (with 1.4 MHz flux density of ~ 164 mJy) we get an opportunity to study the property of the cold H I gas along this dusty sightline. The source is unresolved in the FIRST (Faint Images of Radio Sky at Twenty-centimeter) image with a deconvolved size of $1.32'' \times 0.82''$. As expected, a very strong 21-cm absorption was detected by Giant Metrewave Radio Telescope (GMRT) observations on 02 July 2010 (2 MHz bandwidth split into 128 channels having a velocity resolution of ~ 3.5 km s^{-1} per channel). We obtained a higher resolution (2.08 MHz bandwidth split into 512 channels having a velocity resolution of 0.93 km s^{-1} per channel) GMRT spectrum on 14 and 16 July 2011. All these data were reduced using the National Radio Astronomy Observatory (NRAO) Astronomical Image Processing System (AIPS) following the standard procedures. The radio source is unresolved in our GMRT image (with a spatial resolution of $2.5'' \times 2.1''$) with a peak flux density of 155 mJy/beam. The 21-cm optical depth profile from the high resolution spectrum is shown in Fig. 5. The integrated 21-cm optical depth is found to be, $\mathcal{T} = 15.7 \pm 0.13$ km s^{-1} , with 90% of it is within a velocity range of 28 km s^{-1} (see top panel in Fig. 5). The observed \mathcal{T} translates to $N(\text{H I})$

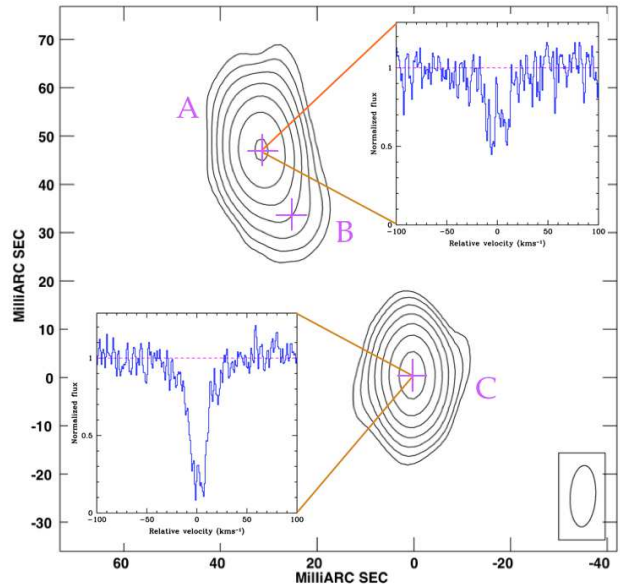


Figure 6. VLBA image showing J1639+1127 resolved into 3 Gaussian components. Crosses mark the locations of components A, B and C from top to bottom. 21-cm H I spectra at the peak of two strongest components, A and C, separated by 89 pc, are also shown. Absorption profiles are clearly different. The RMS in the image is 8.425×10^{-5} Jy/beam and the contour levels are $4.0 \times 10^{-4} \times (-2, -1, 1, 2, 4, 8, 16, 32, \dots)$ Jy/beam. The restoring beam ($0.01271'' \times 0.00533''$ with a position angle is -3.18 deg) is shown as an ellipse at the bottom of the figure. Image center is at RA = 16 39 56.3624 and DEC = +11 27 58.6568.

$= 2.9 \times 10^{19} (T_S/f_c) \text{ cm}^{-2}$ with f_c being the covering factor, the fraction of the background radio emission covered by the absorbing gas. The probable values of $N(\text{H I})$ discussed above based on known correlations suggest that the harmonic mean spin temperature of the H I gas is less than or equal to 100 K as seen in the Galactic ISM.

Another interesting observation is that the H I gas that produces the 21-cm absorption is redshifted with respect to the peak rotational velocity of the H α emitting gas at the same location by up to 25 km s^{-1} (see Fig. 4). This once again confirms that the absorbing gas and H α emitting gas are not co-spatial.

3.2 Spatially resolved VLBA spectroscopy

The VLBA observations of J1639+1127 were carried out on July 27 and October 1, 2011. The total and on-source observing times were 10 and 6.3 hrs respectively. One 8 MHz baseband channel pair was used in these observations, with right- and left-hand circular polarization sampled at 2 bits, and centered at the frequency of the redshifted H I 21-cm line. The data were correlated with 4096 channels (channel width of 0.45 km s^{-1}) and 2 sec correlator integration time. We followed the standard data reduction procedures for reducing the VLBA data (see for example Momjian et al. 2002; Srianand et al. 2012). The radio continuum emission is resolved into multiple components at mas scales (Fig. 6). We use the multiple Gaussian fits to the VLBA images and found 3 distinct components. The results are summarised in

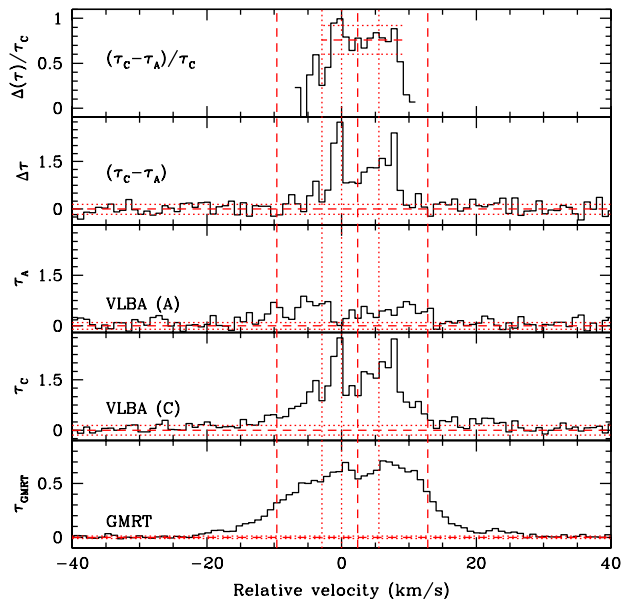


Figure 7. Bottom three panels show the 21-cm optical depth profiles observed in, respectively, the VLBA spectra of components A, C, and the GMRT spectrum. The second panel from the top shows the optical depth difference observed between the two VLBA sightlines. The top panel shows the fractional change in the optical depth between the two sightlines. The velocity scale is defined with respect to $z = 0.079098$. Vertical dashed lines are as defined in Fig. 5 and the dotted lines mark the velocities of narrow components seen towards C.

Table 2. Results of VLBA observations

| Source | Flux density | | Deconvolved | | |
|--------|------------------|--------------|-------------------------------------|-------------|---------------------------------------|
| | Peak mJy/beam | Total mJy | angular size (mas ²) | PA (deg) | $\int \tau(v)dv$ kms ⁻¹ |
| A | 26.8 | 57.4 | 9.9×6.7 | +31.6 | 17.6±1.6 |
| B | 1.7 | 2.1 | 8.8×0.0 [†] | +107.2 | |
| C | 36.8 | 56.8 | 5.9×4.1 | +62.0 | 37.6±2.9 |

[†] An angular extent of 0 indicates a source size much smaller than the synthesized beam.

Table 2. Only 78% of the flux density measured with the GMRT is recovered with the VLBA. Components A and C, that are separated by 55.8 mas (implying a linear line of sight separation of 89 pc at the redshift of the galaxy), have nearly equal flux densities and contribute to 98% of the total flux density seen in the VLBA image. The peak flux densities of these components are 47% and 65% of their respective total flux densities, suggesting structures at few mas scales in the radio emission.

The 21-cm absorption toward the peak emission of A and C extracted from our VLBA observations (smoothed to a channel width of 0.9 km s^{-1} to match the GMRT spectrum) are shown in Fig 6. The integrated 21-cm optical depths, given in the last column of the Table 2, are more than that measured in our GMRT spectrum and differ by a factor of 2 within the 89 pc probed by the two sightlines. Unlike the GMRT spectrum, that is very smooth, the 21-cm spectrum towards component C shows the presence of narrow absorp-

tion components superposed on a smooth absorption profile. This confirms the patchy distribution of the absorbing gas at parsec scales.

To probe this further, we compare in Fig. 7 the optical depth profiles seen in the GMRT and the VLBA observations. Fig. 7 also shows the difference in optical depth (i.e $\Delta\tau$) between the lines of sight towards A and C as a function of velocity. While broad smooth absorption profiles with nearly identical optical depths are seen, narrow absorption components (identified with vertical dotted lines in Fig. 7) are clearly seen only towards C. The top panel of Fig. 7 shows the fractional difference in τ between the two sight lines compared to τ_C . It is clear that on average $\tau_C \sim 5 \times \tau_A$ in the velocity range -5 to 10 km s^{-1} , where the optical depth towards C is dominated by several narrow components. This basically confirms the large variations in H I optical depth over a length scale of 89 pc for narrow H I components.

3.3 Tiny clouds and parsec scale structure

As the deconvolved sizes of the VLBA components correspond to a projected size of $\sim 8 \text{ pc}$ the next question we wish to address is whether there is any optical depth variation over this length scale. We do this by comparing the optical depth profiles seen towards A and C with the total optical depth profile seen in the GMRT spectrum. In general we can write,

$$\tau_{\text{GMRT}}(v) = f_A \tau_A(v) + f_C \tau_C(v) + \tau_D(v). \quad (2)$$

Here, f_A and f_C are the covering factors of the gas component having optical depth $\tau_A(v)$ and $\tau_C(v)$ respectively. $\tau_D(v)$ is the optical depth towards components not seen in the VLBA image. f_C will be 0.37 if the absorbing gas covers all the radio emission seen in the VLBA image from the component C (i.e f_C is ratio of flux density of component C to the total flux density measured in the GMRT image). Therefore, if we assume a plane parallel gas slab covering only the emission from component C then we expect $\tau_{\text{GMRT}}(v) = 0.37\tau_C(v)$. If we assume $\tau_A(v) = \tau_C(v)$, then we expect $\tau_{\text{GMRT}}(v) = 0.74\tau_C(v)$. If $\tau_A(v) \leq \tau_C(v)$ then we expect $0.37 \leq (\tau_{\text{GMRT}}(v)/\tau_C(v)) \leq 0.74$. On the contrary if $\tau_A(v) \geq \tau_C(v)$ then $\tau_{\text{GMRT}}(v)/\tau_C(v) \geq 0.74$. Note this condition is also obtained when additional components are present towards the broad diffuse emission resolved out in the VLBA image (i.e $\tau_D \geq 0$). This discussion clearly suggests that by looking at the ratio of the optical depth observed by GMRT and VLBA in one of the components we will be able to draw broad conclusions about the optical depth variability at small scales.

First we focus on the most interesting narrow component at $v = 0 \text{ km s}^{-1}$. This component is distinctly visible in C and evident even in the GMRT spectrum however clearly absent towards A (as suggested by $\Delta\tau \sim \tau_C$). The peak optical depth of this component is 2.5 ± 0.1 towards C. Based on the flux densities in the VLBA image, if the absorbing gas covers only C then we expect the peak optical depth at $v \sim 0 \text{ km s}^{-1}$ in the GMRT spectrum to be $\sim 0.93 \pm 0.05$. However, the measured value in the GMRT spectrum is 0.70 ± 0.01 , suggesting that, if the absorption component is a plane parallel slab with uniform $N(\text{H I})$, then it would cover only 75% of the continuum emission from component C. The observed parameters, on the contrary simply imply the presence of a

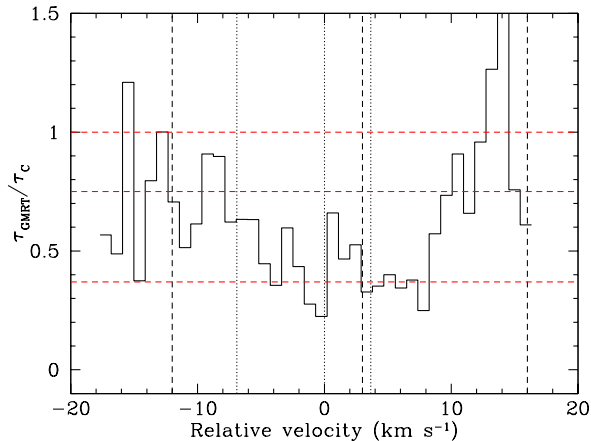


Figure 8. The ratio of τ_{GMRT} and τ_{C} as a function of relative velocity. The velocity scale and vertical lines are as in Fig. 7.

strong optical depth gradient within the deconvolved size of component C (i.e. ≤ 6 mas). This angular scale corresponds to a transverse size < 8.8 pc. As this component is distinctly visible, we fit multiple Gaussian to τ_{C} . While Gaussian fits allow us to get a realistic estimate of FWHM (1.75 km s^{-1}) and the peak optical depth (2.5 ± 0.1) for the narrow component. We get an upper limit of 66 K for the kinetic temperature of the gas from the FWHM. Using this as an indicator of spin temperature (T_{S}), we get $N(\text{H I}) = 5.4 \times 10^{20} (T_{\text{S}}/66\text{K}) \text{ cm}^{-2}$. If we approximate the absorbing cloud as a sphere then we get a particle density of $\sim 40 \text{ cm}^{-3}$ using $N(\text{H I})$ and the transverse size discussed above. Physical conditions in this component are typical of diffuse molecular clouds.

To explore this further we plot in Fig. 8 the ratio of τ_{GMRT} and τ_{C} in the velocity range that contains 90% of the integrated optical depth. The expected ratio when a parallel slab of gas with constant τ covers only the component C, all the VLBA components and all the flux seen by GMRT are shown by horizontal lines at 0.37, 0.74 and 1 respectively. We use this plot to discuss the extent of the gas that produces absorption in different velocity ranges.

First we consider the velocity range $3 \leq v(\text{km s}^{-1}) \leq 9$ where absorption is seen towards both A and C with $\tau_{\text{C}} \sim 5 \times \tau_{\text{A}}$ (see top panel in Fig. 7). If the gas towards C and A covers all the radio emission from these components then we expect $\tau_{\text{GMRT}}/\tau_{\text{C}}$ to be 0.44 (i.e. $0.37 \times (1.0 + 0.2)$). From Fig. 8 we see the observed ratio is consistent with 0.38 in this range. We notice that the optical depth error in each channel in the VLBA spectrum towards C is ~ 0.1 . For the mean optical depth measured in this velocity range this translate to an error of 0.03 in the ratio. Therefore, in each channel we find the ratio to be lower than 0.44 by 2σ level. As this happens over 6 channels we see the difference to be significant at the 4.8σ level. This difference can be understood if some of the narrow components seen towards C have projected sizes less than 8.8 pc (or the presence of strong opacity gradient within this scale) as seen in the case of the narrow component at $v \sim 0 \text{ km s}^{-1}$.

In the velocity ranges $10 \leq v(\text{km s}^{-1}) \leq 16$ and $-10 \leq v(\text{km s}^{-1}) \leq -4$ from Fig.7, we find $\Delta\tau \sim 0$. Therefore we expect the ratio of τ_{GMRT} and τ_{C} to be 0.74. In the case

of the first velocity range the ratio is above 0.74. In the framework presented above, this could either mean $\tau_{\text{A}} \geq \tau_{\text{C}}$ or contribution to τ_{GMRT} from the diffuse component resolved in the VLBA image. If we use the average value (1.2) of the measured ratio in this velocity range we get $\tau_{\text{A}} = 2.1 \times \tau_{\text{C}}$. In the second velocity interval the ratio is found to be between 0.36 and 0.74. This is consistent with $\tau_{\text{A}} \leq \tau_{\text{C}}$. Using the mean value of the ratio (0.65) in this velocity range we find $\tau_{\text{c}} \sim 1.4\tau_{\text{A}}$. These are very different from $\tau_{\text{C}} = \tau_{\text{A}}$ we see towards the peak emission in A and C. Therefore, we can conclude that there are strong opacity gradients at the spatial scale of ~ 10 pc even in the gas that produces absorption in this velocity range.

Finally in the velocity range -18 to -10 km s^{-1} , the absorption profile is smooth both in the VLBA spectrum towards C and the GMRT spectrum. Therefore we smooth the spectra to a 4 km s^{-1} resolution to increase the signal to noise ratio. We notice that $\tau_{\text{GMRT}}/\tau_{\text{C}}$ in this velocity range is 0.67 ± 0.03 . This just differs from the expected value of 0.74 by 2.3σ level. Within the observational uncertainty the optical depth seen towards A and C are nearly equal as suggested by the difference in τ plotted in Fig. 7. Increasing the signal to noise of our VLBA spectra will help detecting minor optical depth differences even in this smooth component.

In summary, we find the 21-cm absorption has both narrow and broad components. The narrow components show optical depth variations by a factor 1.4 to 10 over a 89 pc scale. In one of the narrow components we show that optical depth variations are present over a 8 pc scale. On the contrary the absorption seen in the broad wings are consistent with nearly similar optical depths (i.e at 2.5σ level) within measurement uncertainty. Thus a simple picture of the system could be that of several cold, dense and small clouds with characteristic size ≤ 10 pc embedded in a smooth diffuse H I medium covering several tens of parsec. This scenario is similar to the ‘‘blobby sheets’’ seen in the Galactic ISM (Heiles & Troland 2003).

4 DISCUSSION

We report the detection of diffuse interstellar bands and 21-cm absorption from the $z_{\text{abs}} = 0.079$ galaxy SDSS J163956.38+112802.1 towards the $z_{\text{em}} = 0.993$ QSO J163956.35+112758.7. The QSO line of sight in this case is passing through the disk of a relatively low mass ($\sim 4 \times 10^{10} M_{\odot}$), near solar metallicity spiral galaxy at an impact parameter of ~ 4 kpc. The region with highest star formation surface density, inferred from $H\alpha$ emission, in this galaxy is located within a projected distance of 0.7 kpc from the QSO sightline.

The QSO is highly reddened with $E(\text{B-V}) \sim 0.83 \pm 0.11$ (estimated from the SED fitting) along the line of sight. This suggests that the line of sight is passing through a translucent interstellar medium. The measured $E(\text{B-V})$, rest equivalent widths of Na D lines and surface density of star formation favor $N(\text{H I}) \geq 10^{21} \text{ cm}^{-2}$ along this sight line.

We report the detection of a $\lambda 6284$ DIB feature in the QSO spectra at the redshift of the galaxy. The strength of this feature per unit reddening is found to be higher than what is seen in the Milkyway. This could be related to dif-

ferences in the DIB carrier and/or to the ambient radiation field. We also find the FWHM of this feature to be broader than what is typically seen in our Galaxy but close to what is seen in starburst galaxies. Our spectrum is consistent with the presence of the $\lambda 5780$ DIB with a rest equivalent width predicted from the observed $\lambda 6284$ DIB feature and the correlation reported by Friedman et al. (2011). Due to poor SNR, no other DIB feature is detected in our spectrum. In order to probe the physical conditions and the nature of the DIB carriers it would be important to obtain high signal-to-noise ratio spectrum of the QSO.

Strong 21-cm absorption from the galaxy, spread over 28 km s^{-1} , is detected in our GMRT spectrum. Our follow-up VLBA observations reveal the presence of two strong radio emitting components, separated by 89 pc, that are used to understand the spatial variations of the 21-cm optical depth. First we notice that the integrated optical depths towards these two components differ by a factor of 2. We show that this difference is mainly dominated by narrow components that are seen only towards one of the VLBA component (i.e. component C). In these narrow components the H I opacity seems to change over ~ 10 pc scales. For one of these narrow components we show the kinetic temperature is ≤ 66 K. As we expect dust to be mainly associated with low temperature gas, if the other narrow components are also cold, then we can speculate that the optical emission from the QSO is associated with the VLBA component C.

In high- z 21-cm absorption line studies of DLAs and Mg II systems, and in the absence of VLBI spectroscopy, one uses the ‘core’ fraction measured from the mas scale continuum images to correct the optical depths for partial coverage (see for example, Kanekar et al. 2009; Srianand et al. 2012; Gupta et al. 2012). In case of DLAs, this allows one to measure the spin temperature of the H I gas. There are three issues that affect this approach: (i) Unambiguous identification of the ‘core’. If the milliarcsecond morphology of the radio emission is not simple, then VLBI observations are needed to identify the flat-spectrum ‘core’ component. (ii) The fact that the radio sight line towards the ‘core’ may still be tracing a larger gas volume with respect to the optical sight line. (iii) The implicit assumption that a single absorbing cloud covers the ‘core’ i.e. a single covering factor (f_c).

The third issue is mainly related to the patchiness of the absorbing gas on scales of tens of pc, which is typically the resolution provided by VLBI observations, and can only be addressed via VLBI spectroscopy. In the case of J1639+1127 discussed here it is plausible to associate component C with the quasar sight line because it shows clear signatures of the presence of a large amount of cold gas. Under the assumption of a single cloud covering C we would have estimated f_c as 0.37 (57/155). However, if some of the absorption components were to cover only the peak of C, then f_c would be off by as much as a factor of 1.5 (56.8/36.8) from the above value. Furthermore, the covering factor estimate could be dramatically off if the core is associated with component B, resulting in f_c of 0.01, or with a component not detected in our VLBA image. This is a possibility considering that the radio continuum morphology of J1639+1127 at high angular resolution (see Fig 6) resembles that of a compact symmetric object (CSO; Conway 2002). Here, the two dominant radio sources, A and C, would be the two radio lobes of the CSO.

Therefore, multi-frequency VLBI observations are needed to detect and/or identify the core component to address this issue.

The case of J1639+1127 also demonstrates that associating the entire absorption detected at arcsecond scales through GMRT observations with either A or C component would lead to f_c estimates that are at least off by a factor of 2. In general, this means that even when the core component is accurately identified, T_S measurements from DLA studies can have large errors especially if the background quasar has significant radio structure at the scales where the absorbing gas has strong optical depth gradients. Therefore one requires more high- z measurements towards strong core dominated sources to address the issues related to the measurements of T_S .

Based on the measured E(B-V), the equivalent widths of $\lambda 6284$ DIB and Na D lines and various correlations found in our Galaxy we predict appreciable column densities of molecular species like CH, CH^+ and CN along this line of sight. Detecting these species will allow us to probe the physical and chemical state of this translucent gas in detail. In addition, this is a good target to search for OH lines and molecular lines in radio/mm wavebands.

5 ACKNOWLEDGEMENTS

We thank the referee and Pushpa Khare for useful comments. We thank GMRT and VLBA staff for their support during the observations. The VLBA is run by National Radio Astronomy Observatory. The VLBA data were correlated using NRAO implementation of the DiFX software correlator (Deller et al. 2011) that was developed as part of the Australian Major National Research facilities Programme and operated under license. The National Radio Astronomy Observatory is a facility of the National Science Foundation operated under cooperative agreement by Associated Universities, Inc. GMRT is run by the National Centre for Radio Astrophysics of the Tata Institute of Fundamental Research. We acknowledge the use of SDSS spectra from the archive (<http://www.sdss.org/>). R.S. and P.P.J. gratefully acknowledge support from the Indo-French Centre for the Promotion of Advanced Research (Centre Franco-Indien pour la promotion de la recherche avance) under Project N.4304-2.

REFERENCES

- Balashev S. A., Petitjean P., Ivanchik A. V., Ledoux C., Srianand R., Noterdaeme P., Varshalovich D. A., 2011, MNRAS, pp 1400–
- Bates B., Shaw C. R., Kemp S. N., Keenan F. P., Davies R. D., 1995, ApJ, 444, 672
- Böhlín R. C., Savage B. D., Drake J. F., 1978, ApJ, 224, 132
- Boissé P., Le Petit F., Rollinde E., Roueff E., Pineau des Forêts G., Andersson B.-G., Gry C., Felenbok P., 2005, A&A, 429, 509
- Borthakur S., Tripp T. M., Yun M. S., Bowen D. V., Meiring J. D., York D. G., Momjian E., 2010, ArXiv e-prints

- Brogan C. L., Zauderer B. A., Lazio T. J., Goss W. M., DePree C. G., Faison M. D., 2005, *AJ*, 130, 698
- Conway J. E., 2002, *New A Rev.*, 46, 263
- Cordiner M. A., Cox N. L. J., Evans C. J., Trundle C., Smith K. T., Sarre P. J., Gordon K. D., 2011, *ApJ*, 726, 39
- Cordiner M. A., Smith K. T., Cox N. L. J., Evans C. J., Hunter I., Przybilla N., Bresolin F., Sarre P. J., 2008, *A&A*, 492, L5
- Cox N. L. J., Cordiner M. A., Cami J., Foing B. H., Sarre P. J., Kaper L., Ehrenfreund P., 2006, *A&A*, 447, 991
- Cox N. L. J., Cordiner M. A., Ehrenfreund P., Kaper L., Sarre P. J., Foing B. H., Spaans M., Cami J., Sofia U. J., Clayton G. C., Gordon K. D., Salama F., 2007, *A&A*, 470, 941
- Deller A. T., Brisken W. F., Phillips C. J., Morgan J., Alef W., Cappallo R., Middelberg E., Romney J., Rottmann H., Tingay S. J., Wayth R., 2011, *PASP*, 123, 275
- Deshpande A. A., 2000, *MNRAS*, 317, 199
- Ellison S. L., York B. A., Murphy M. T., Zych B. J., Smith A. M., Sarre P. J., 2008, *MNRAS*, 383, L30
- Ferlet R., Vidal-Madjar A., Gry C., 1985, *ApJ*, 298, 838
- Fitzpatrick E. L., Massa D., 1988, *ApJ*, 328, 734
- Frail D. A., Weisberg J. M., Cordes J. M., Mathers C., 1994, *ApJ*, 436, 144
- Friedman S. D., York D. G., McCall B. J., Dahlstrom J., Sonnentrucker P., Welty D. E., Drosback M. M., Hobbs L. M., Rachford B. L., Snow T. P., 2011, *ApJ*, 727, 33
- Gupta N., Srianand R., Bowen D. V., York D. G., Wadadekar Y., 2010, *MNRAS*, 408, 849
- Gupta N., Srianand R., Petitjean P., Bergeron J., Noterdaeme P., Muzahid S., 2012, *A&A*, 544, A21
- Heckman T. M., Lehnert M. D., 2000, *ApJ*, 537, 690
- Heiles C., 1997, *ApJ*, 481, 193
- Heiles C., Troland T. H., 2003, *ApJ*, 586, 1067
- Hobbs L. M., York D. G., Snow T. P., Oka T., Thorburn J. A., Bishof M., Friedman S. D., McCall B. J., Rachford B., Sonnentrucker P., Welty D. E., 2008, *ApJ*, 680, 1256
- Jiang P., Ge J., Zhou H., Wang J., Wang T., 2011, *ApJ*, 732, 110
- Junkkarinen V. T., Cohen R. D., Beaver E. A., Burbidge E. M., Lyons R. W., Madejski G., 2004, *ApJ*, 614, 658
- Kanekar N., Chengalur J. N., 2001, *MNRAS*, 325, 631
- Kanekar N., Chengalur J. N., 2003, *A&A*, 399, 857
- Kanekar N., Lane W. M., Momjian E., Briggs F. H., Chengalur J. N., 2009, *MNRAS*, 394, L61
- Kennicutt Jr. R. C., 1998a, *ARA&A*, 36, 189
- Kennicutt Jr. R. C., 1998b, *ApJ*, 498, 541
- Komatsu E., Dunkley J., Nolte M. R., Bennett C. L., Gold B., Hinshaw G., Jarosik N., Larson D., Limon M., Page L., Spergel D. N., Halpern M., Hill R. S., Kogut A., Meyer S. S., Tucker G. S., Weiland J. L., Wollack E., Wright E. L., 2009, *ApJS*, 180, 330
- Lane W. M., Briggs F. H., Smette A., 2000, *ApJ*, 532, 146
- Ledoux C., Petitjean P., Srianand R., 2003, *MNRAS*, 346, 209
- Mac Low M.-M., Klessen R. S., 2004, *Reviews of Modern Physics*, 76, 125
- McKee C. F., Ostriker J. P., 1977, *ApJ*, 218, 148
- Momjian E., Romney J. D., Troland T. H., 2002, *ApJ*, 566, 195
- Noterdaeme P., Ledoux C., Petitjean P., Srianand R., 2008, *A&A*, 481, 327
- Noterdaeme P., Ledoux C., Srianand R., Petitjean P., Lopez S., 2009, *A&A*, 503, 765
- Osterbrock D. E., Ferland G. J., 2006, *Astrophysics of gaseous nebulae and active galactic nuclei*
- Pettini M., Pagel B. E. J., 2004, *MNRAS*, 348, L59
- Poznanski D., Prochaska J. X., Bloom J. S., 2012, *ArXiv e-prints*
- Rollinde E., Boissé P., Federman S. R., Pan K., 2003, *A&A*, 401, 215
- Roy N., Chengalur J. N., Srianand R., 2006, *MNRAS*, 365, L1
- Roy N., Minter A. H., Goss W. M., Brogan C. L., Lazio T. J. W., 2012, *ApJ*, 749, 144
- Sarre P. J., 2006, *Journal of Molecular Spectroscopy*, 238, 1
- Snow T. P., McCall B. J., 2006, *ARA&A*, 44, 367
- Sollerman J., Cox N., Mattila S., Ehrenfreund P., Kaper L., Leibundgut B., Lundqvist P., 2005, *A&A*, 429, 559
- Srianand R., Gupta N., Petitjean P., Noterdaeme P., Ledoux C., Salter C. J., Saikia D. J., 2012, *MNRAS*, 421, 651
- Srianand R., Noterdaeme P., Ledoux C., Petitjean P., 2008, *A&A*, 482, L39
- Srianand R., Petitjean P., Ledoux C., Ferland G., Shaw G., 2005, *MNRAS*, 362, 549
- Turnshek D. A., Rao S., Nestor D., Lane W., Monier E., Bergeron J., Smette A., 2001, *ApJ*, 553, 288
- van Dishoeck E. F., Black J. H., 1989, *ApJ*, 340, 273
- Wakker B. P., Mathis J. S., 2000, *ApJ*, 544, L107
- Wang X., Wang L., Pain R., Zhou X., Li Z., 2006, *ApJ*, 645, 488
- Welty D. E., Federman S. R., Gredel R., Thorburn J. A., Lambert D. L., 2006, *ApJS*, 165, 138
- Wild V., Kauffmann G., Heckman T., Charlot S., Lemson G., Brinchmann J., Reichard T., Pasquali A., 2007, *MNRAS*, 381, 543
- Wolfe A. M., Briggs F. H., Davis M. M., 1982, *ApJ*, 259, 495
- York B. A., Ellison S. L., Lawton B., Churchill C. W., Snow T. P., Johnson R. A., Ryan S. G., 2006, *ApJ*, 647, L29